# Advanced flow profiler for two-phase flow imaging on distillation trays

Vishwakarma, V.; Schleicher, E.; Bieberle, A.; Schubert, M.; Hampel, U.;

# Advanced flow profiler for two-phase flow imaging on distillation trays

Vineet Vishwakarma[a,b,*], Eckhard Schleicher[a], André Bieberle[a], Markus Schubert[a,*], and Uwe Hampel[a,b]

[a]Institute of Fluid Dynamics, Helmholtz-Zentrum Dresden-Rossendorf, Bautzner Landstraße 400, 01328 Dresden, Germany

[b]Chair of Imaging Techniques in Energy and Process Engineering, Technische Universität Dresden, 01062 Dresden, Germany

*Corresponding authors: m.schubert@hzdr.de (M. Schubert)

v.vishwakarma@hzdr.de (V. Vishwakarma)

**Abstract:** A profound knowledge of the two-phase cross-flow on large-scale distillation trays is pivotal to their efficient design and operation. For such trays, a novel flow profiler comprising multiple dual-tip probes for simultaneous local conductivity measurements is proposed in this work. The profiler is applied for a DN800 air/water column simulator equipped with sieve trays. 3D distribution of liquid holdup and tracer-based liquid flow in the two-phase dispersion are assessed in high resolution. Non-uniform holdup is found along the dispersion height. Contrarily, the liquid flow is largely uniform and symmetric with respect to the tray centerline. Prior to measurements, the profiler design, electronic scheme, measurement principle and data processing schemes are described.

**Keywords:** column tray, two-phase cross-flow, 3D flow imaging, conductivity measurement, liquid holdup, tracer dispersion.

## 1. Introduction

Two-phase flow distribution on distillation column trays has considerable influence on their fractionating performance.[1-3] These energy-demanding columns are considered as cascades of trays that are geometrically and functionally similar.[4] A detailed understanding of fluid dynamics on individual trays would allow estimating the column performance accurately as well as optimizing the flow profiles through design revamps.[5-7]

Among various tray configurations, cross-flow sieve trays are probably the most often used ones in distillation columns.[8] Here, liquid flows horizontally over the perforated area of the tray called as deck. Coincidentally, vapor rises upwards through the flowing liquid via deck perforations. The cross-flow contact of liquid and vapor over the deck results in a complex two-phase dispersion,[2,9] whose characteristics depend on the evolving flow regimes[10-12] as a result of system properties as well as tray and column design and operating conditions.[5,13-15] Froth and spray are the most common regimes, where liquid is the continuous phase and gas is the dispersed phase, and vice-versa. Such regimes are commonly identified via time-averaged liquid fraction measurements at various locations above the tray deck (i.e., on a plane orthogonal to the main liquid flow direction) for example using γ-ray attenuation technique,[11,16-20] which can be expensive and cumbersome. Conductivity[17,21] and optical[22] probes have also been used to study local bubble characteristics in the two-phase environment. All these techniques have only reported the experimental data at selective tray locations and planes in either small or rectangular columns, where the flow distribution differs from that of an industrial-scale column. Thus, full 3D characterization of the two-phase flow on an industrial-scale distillation tray is not yet available in the literature.

A particular aspect of the tray hydrodynamics is flow maldistribution with respect to a desirable uniform and unidirectional flow.[23] Possible types of liquid maldistribution on cross-flow trays are channeling, bypassing, recirculation and stagnant zones.[4,24] Such non-uniform flow profiles are detrimental to the tray efficiency depending upon their extent of maldistribution.[3-6,24-26]

**Table 1.** Experimental techniques for liquid flow visualization on column trays.

| Technique | System | Tray diameter and deck |
|---|---|---|
| Photographic camera (dye tracer)[14] | air – water | 1.22 m, sieve |
| Cork floats[27] | air – water | 0.50 m, sieve |
| Fiber-optic probe network (dye tracer)[15] | air –water | 1.21 m, sieve |
| Thermocouple network[28] | air – hot water | 2.30 m, sieve and bubble-cap |
| Strain gauge probe network[6] | air –water | 1.80 m, sieve |
| Conductivity probes (salt tracer)[29] | air – water | 2.00 m, sieve |
| Network of thermometers and flow pointers[25] | air – hot water | 2.44 m, sieve |
| Hot film anemometer[30] | air – water | 1.20 m, sieve |
| Infrared camera (hot water as tracer)[24] | air – water | 1.20 m, sieve (double-pass) |
| Conductivity-based wire-mesh sensor (salt tracer)[5] | air – water | 0.80 m, sieve |

The chaotic and 3D behavior of two-phase flow on industrial-scale column trays poses serious challenges in identifying flow patterns accurately.[2,31] The techniques used in the past to quantify liquid flow patterns on the trays are summarized in Table 1. Simplified, they can be categorized into float application, camera visualizations and point measurements (or networks of these), and have succeeded in recognizing gross maldistribution. However, the floats can only roughly indicate the real flow at the dispersion surface. Similarly, the camera measurements can also reveal the liquid flow near the dispersion surface only. On the other hand, the point measurements suffer from a variety of limitations such as high invasiveness, challenging calibration scheme, signal interference, low spatial resolution, and so forth. Single or small arrays of probes also demand significant mechanical effort, complex electronic schemes and high measurement time to acquire 3D data. A detailed review of these techniques and their application in tray columns can be found elsewhere.[4]

In this work, a novel multiplex flow profiler for 3D measurements of liquid holdup distributions is exemplified for a sieve tray. Additionally, liquid flow patterns are quantified using this profiler via tracer pulse injection. In particular, the design characteristics of the new profiler, associated electron-

ics, measurement principle, reference framework as well as the data processing schemes are discussed. This work focusses on demonstrating the versatile capabilities of the new profiler regarding the two-phase cross-flow measurements.
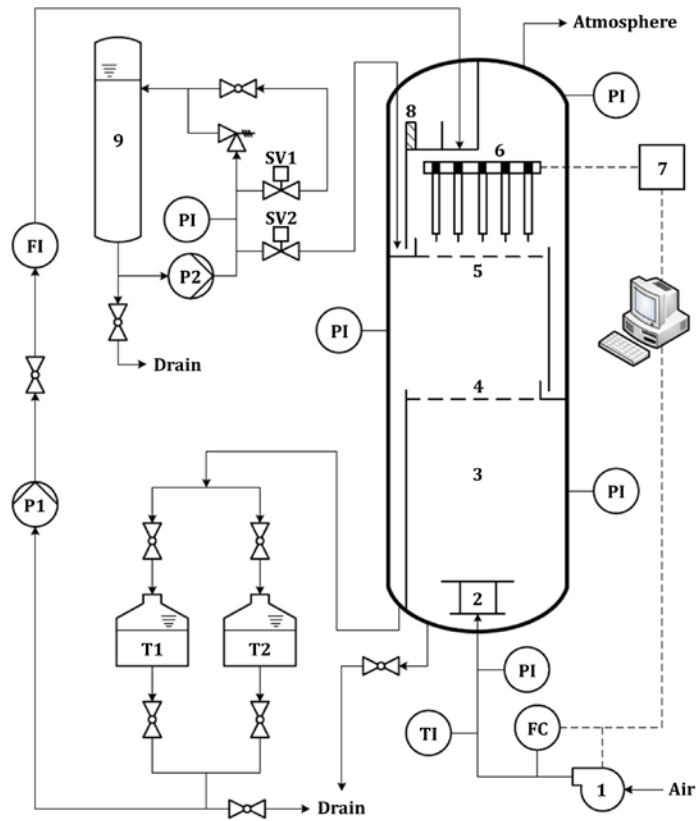


**Figure 1.** Schematic diagram of the experimental facility (1 – air blower, 2 – air distributor, 3 – tray column, 4,5 – sieve trays, 6 – multiplex profiler, 7 – profiler electronics, 8 – mesh distributor, 9 – tracer batch, FC – flow controller, FI – flow indicator, PI – pressure indicator, P1, P2 – centrifugal pumps, SV1, SV2 – solenoid valves, TI – temperature indicator, and T1, T2 – tap water tanks).

## 2. Experimental setup

A schematic diagram of the column mock-up and instrumentation is shown in Fig. 1. The column (ID of 800 mm) comprises three flange-mounted segments that are 735 mm, 375 mm and 860 mm high

from top to bottom. Two identical sieve trays of 15 mm thick PMMA are installed between the segments with an effective tray spacing of 365 mm. Each tray has 3052 holes of 5 mm diameter resulting in a fractional free area of 13.55%. The column and tray specifications are summarized in Table 2.

**Table 2.** Column and sieve tray dimensions.

| Component | Dimensions |
| --- | --- |
| Internal column diameter | 800 mm |
| Hole specifications | 3052 × 5 mm Ø, pitch: Δ × 12 mm |
| Inlet weir (L × W × H) | 532 mm × 2 mm × 35 mm |
| Outlet weir (L × W × H) | 465 mm × 2 mm × 20 mm |
| Flow path length | 620 mm |
| Active tray area | 0.44 m² |
| Fractional free area | 13.55% |
| Downcomer clearance | 20 mm |
| Tray spacing | 365 mm |
| Tray thickness | 15 mm |
| Calming zone | 36 mm (inlet), 30 mm (outlet) |

Air and tap water are used as gas and liquid phases, respectively. An adjustable high-pressure blower is used for supplying air to the column. The distributor disperses the air across the active tray area uniformly. Water is supplied to the column top from two 1 m³ tanks by a centrifugal pump and regulated and monitored via ball valve and rotameter, respectively. The liquid exiting from the column bottom is recycled back hydrostatically to the tanks. In this work, liquid and gas loads for the column are selected as 2.26 m³/(m²h) and 1.95 Pa$^{0.5}$, respectively. It is necessary that the column attains steady state prior to any experimentation, which ensures uniform temperature and electrical conductivity of the liquid.

Deionized water is used as tracer. Its low electrical conductivity and nearly identical physical properties compared with tap water makes it an ideal tracer. Upon actuating the solenoid valve SV2, the pump P2 pushes a certain tracer quantity via 16 identical sub-pipes (in a binary tree arrangement) to

the downcomer clearance. Consecutive trials showed a uniform tracer injection with an average tracer discharge of 1.38 l/s in all sub-pipes for valve actuation times of 1 s, 2 s and 3 s, respectively.

## 3. Multiplex flow profiler

The liquid holdup and velocity distributions of the two-phase cross-flow on the sieve tray are determined based on multiple local data obtained with a novel multiplex flow profiler.[32,33] This profiler mainly comprises 4 components namely supporting grid, measuring probes, holding frame and electronics as shown in Fig. 2. The supporting grid consists of two sets of printed circuit boards (PCBs), referred to as transmitter and receiver headers for electrically connecting the probes. Those headers have equidistant notches that allow arranging them orthogonally and forming a mechanically stable matrix of headers over the active tray area (Fig. 2a). This skeletal grid ensures negligible obstruction to the outflowing air. 28 transmitter headers (21 mm lateral distance) and 32 receiver headers (24 mm lateral distance) are used in the supporting grid that holds 776 dual-tip probes. Each probe is an identical multilayer PCB whose scheme and dimensions are illustrated in Fig. 2b. There are three parallel copper sheets inside the probe that are separated and enclosed by insulating sheaths. The outward sheets are electrically connected to transmitter and receiver headers, individually. The middle sheet acting as shielding is connected to the ground potential. Electromagnetic shielding and insulation prevent any current flow between transmitter and receiver sheets inside the probe. All soldered joints in the supporting grid are covered with an epoxy layer to prevent any corrosion caused by the liquid as well as for insulation. The probe tail has two small connecting pads corresponding to each transmitter and receiver sheet. Two identical steel electrodes of 0.5 mm diameter are soldered to each of those pads, and the effective length of the electrodes from the probe tail is 10 mm. Those electrodes are insulated up to 8 mm length with a Teflon layer, and thus, rendering only the tip of the electrodes exposed to the gas-liquid flow. The probe tips are
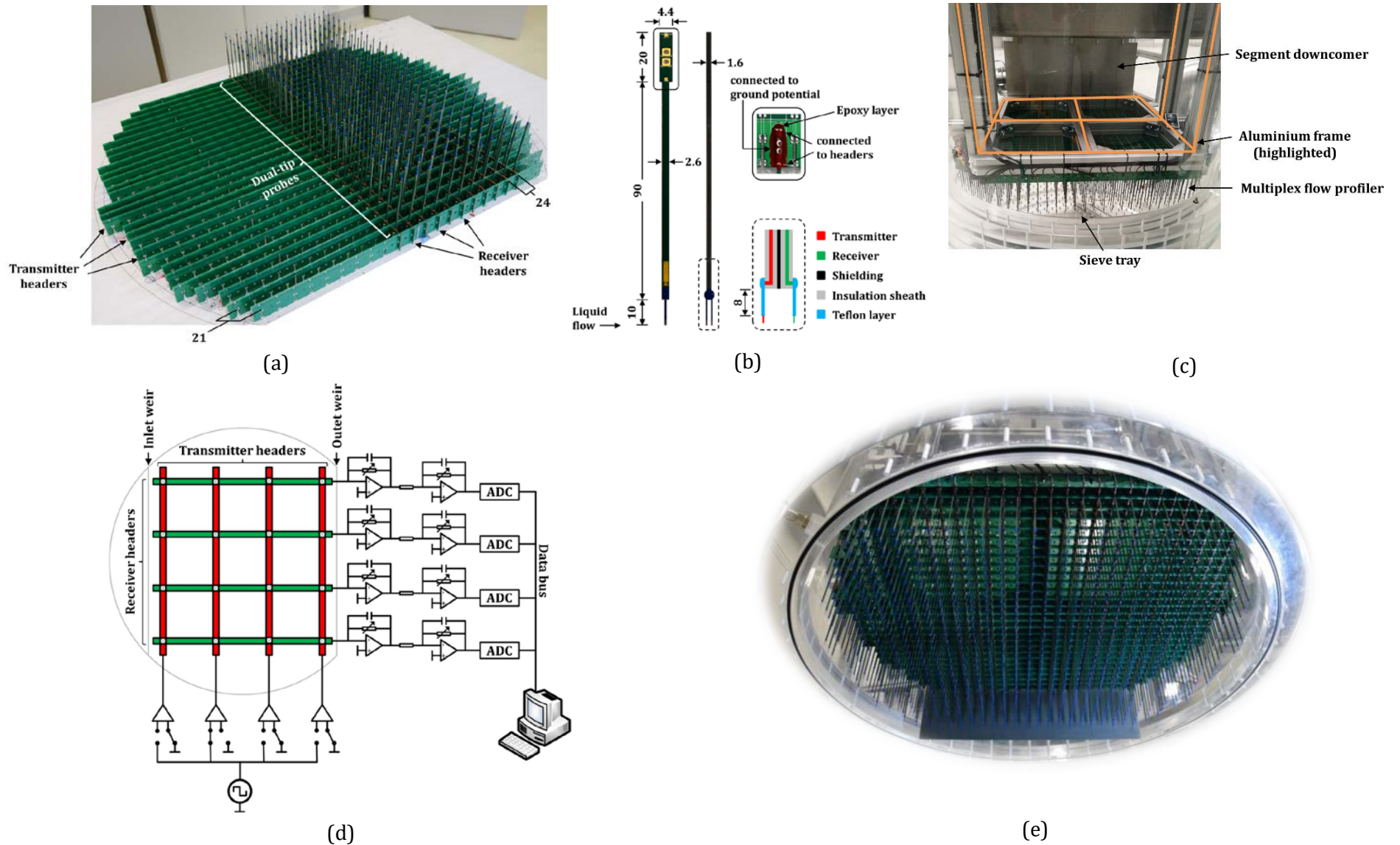
**Figure 2.** Multiplex flow profiler arrangement: (a) supporting grid (during construction phase), (b) details and dimensions of a probe, (c) holding frame, (d) electronic scheme (exemplarily shown for a 4 x 4 arrangement), (e) profiler assembly inside the column.

positioned orthogonally to the main liquid flow direction. Overall insulation and shielding in the profiler avoids cross talk and large capacitance buildup, which favors simple calibration and data processing. Eventually, the supporting grid with the probes is mounted on an aluminum frame (Fig. 2c), and its elevation above the tray can be adjusted manually.

The schematic diagram of the profiler electronics is exemplarily shown for a 4 × 4 grid in Fig. 2d, where the excitation voltage is applied to each transmitter header sequentially via multiplexing scheme. Based on the local instantaneous conductance between the electrode tips, an electrical current flowing towards the receiver tips is recorded by parallel sampling of the receiver headers. If the local control volume between the transmitter and receiver of a probe is occupied by liquid, then the current continues to flow unless the gas exchanges the liquid in that volume. This way, each probe measures the temporal variation of the presence of liquid and gas locally. The maximum temporal resolution is 5000 Hz for the given 28 × 32 profiler configuration.

The received current is then processed and amplified via one trans-impedance amplifier and one voltage amplifier in series. The resulting voltage signals are digitized into 12-bit digital values (ranging between 0 and 4095) using analog-to-digital converters (ADCs). Subsequently, these digital values are stored as 16-bit values by inserting four leading zeros. The digital data containing ADC values are further processed in MATLAB (R2017b) for quantifying the distributions of liquid holdup and residence time (see Sections 4 and 5).

Fig. 2e shows the profiler installed inside the column. With this arrangement, an array of short sensing tips ensures precise planar measurements simultaneously at 776 local positions with low intrusiveness to the flow. Vertical traversing of the profiler allows 3D flow visualization. The local liquid velocities can also be easily determined via tracer flow data at multiple tray locations.
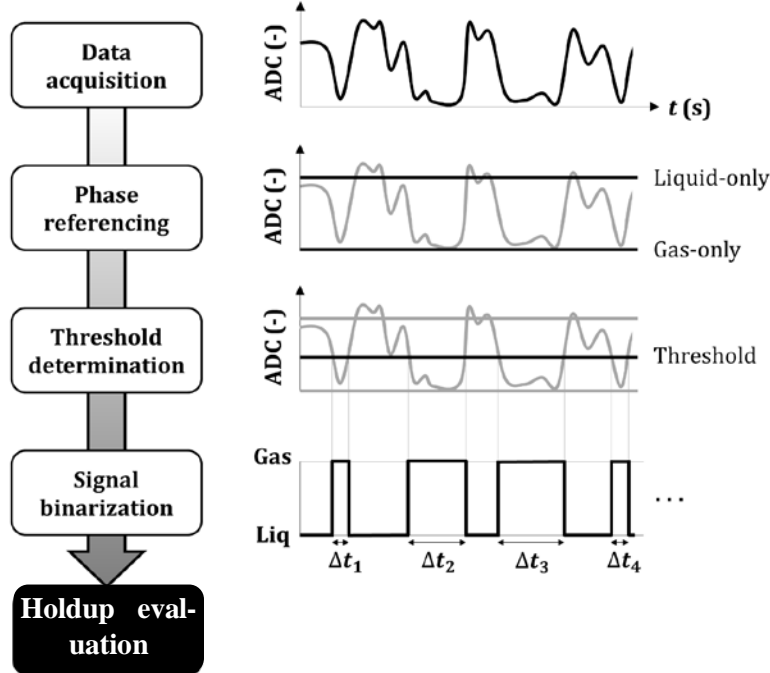
**Figure 3.** Sequence of steps for the holdup calculation.

## 4. 3D holdup assessment

Fig. 3 illustrates the series of steps along with their illustration that are involved in calculating the local liquid holdup at each probe location. The first step is the acquisition of the ADC time-series values pertaining to the two-phase flow followed by obtaining the characteristic ADC values corresponding to the liquid and gas phase referred to as phase referencing. Then, a threshold (defined as a certain percentage of the difference between ADC values of liquid-only and gas-only) is determined that permits discretizing the two-phase signal as displayed in Fig. 3. The resulting binary signal reveals the time instances of the exposure of a probe to either gas or liquid in the two-phase cross-flow.[34] By summing up the periods of the gas contact, the local time-averaged gas holdup ($\varepsilon$) can be calculated as

$$\varepsilon_{x,y} = \frac{\sum_z \Delta t_{x,y,z}}{t_{\text{total}}} \quad . \tag{1}$$

Here, $\Delta t_{x,y,z}$ are the periods of the gas contact in $z$ instances for the probe $[x, y]$, and $t_{\text{total}}$ is the total measurement time. Eventually, the local time-averaged liquid holdup $(\alpha)$ can be obtained as

$$\alpha_{x,y} = 1 - \varepsilon_{x,y} \quad . \tag{2}$$

## 4.1. Data acquisition

Firstly, the flow profiler is positioned at 20 mm above the tray deck (i.e., the lowest elevation here) and acquires the two-phase response for $t_{\text{total}} = 300$ s at the maximum frequency of 5000 Hz. Then, it is elevated up to 100 mm above the tray in the steps of 10 mm, and the data recording is repeated at each step. The ADC response at each elevation is structured into a 3D matrix of size 32 × 28 × 1500000 (i.e., $[x, y, g_{\text{total}}]$) for subsequent data processing in MATLAB (R2017b). For instance, the ADC value time-series signals of the probe [17,17] at different elevations are shown in Fig. 4. As expected, the two-phase characteristics vary at different heights above the tray.

## 4.2. Phase referencing

The characteristic ADC values for liquid and gas phases are normally derived from the ADC value histograms that largely exhibit bimodal distribution. However, the liquid-only peaks (see Figs. 4a-c) vary because of the complex distribution of liquid in the form of lumps, films and droplets. Thus, the liquid ADC data from the profiler fully immersed in liquid (refer to Fig. 4d) and ADC = 0 are used for liquid-only and gas-only values, respectively, that are required for signal discretization. A variation in liquid-only ADC values can be seen in Fig. 4b, because of the tiniest geometric variations in the measuring probes as well as the small deviations in the components (such as resistor, trans-impedance amplifier, voltage amplifier, ADC, and so forth) along the electronic chain for each signal channel. It should be noted that temperature and electrical conductivity of the liquid (i.e., 17.5 °C and 318 μS/cm, respectively) were kept constant during two-phase ADC recording.

### 4.3. Threshold determination

A single-threshold method is adopted for every probe of the profiler, which is the most common and robust phase discrimination technique.[35] According to the sequence of steps shown in Fig. 3, a threshold value can be back-calculated if the holdup is already known. In this regard, the two-phase flow in a small-scale tray column (ID 100 mm) is subjected to γ-ray computed tomography (CT) for holdup distribution measurements. Simultaneously, a reduced 3 × 3 profiler is employed inside the column as a counterpart of the actual 28 × 32 profiler with the same technical specifications. Following the back-calculation approach for the downscaled profiler, a threshold equal to 75% (of the liquid-only ADC values at each probe) gives the lowest relative deviation (i.e., below 10%) with respect to the CT-led holdup data. A complete description of the small-scale setup, liquid and gas loading, CT measurement, and profiler application for the threshold determination is provided in Section S1 of the Supplementary Information.

### 4.4. Signal binarization

Prior to the holdup calculation according to Eqs. 1 and 2, the data signal of each probe is binarized as illustrated in Fig. 3. This is exemplarily shown for probe [17,17] in Fig. 5. It should be noted that the corresponding data are already displayed in Fig. 4. In the binary data, the relative occurrence of liquid and gas exposure at the electrode tips is a measure that characterizes the local two-phase fluid dynamics. Fig. 5a shows that the liquid content in the local two-phase mixture is comparably lower at 20 mm height above the tray. At this elevation, the electrodes are largely exposed to the gas phase that expectedly oscillates between irregular jets and bubbles in the intermittent periods. Coincidentally, the gas jets fragment the surrounding liquid and project those fragments upwards reducing the local liquid content. Fig. 5b indicates that the gas jets are broken into less erratic shapes at 40 mm elevation because of the shearing flow of liquid. At this elevation, a majority of the
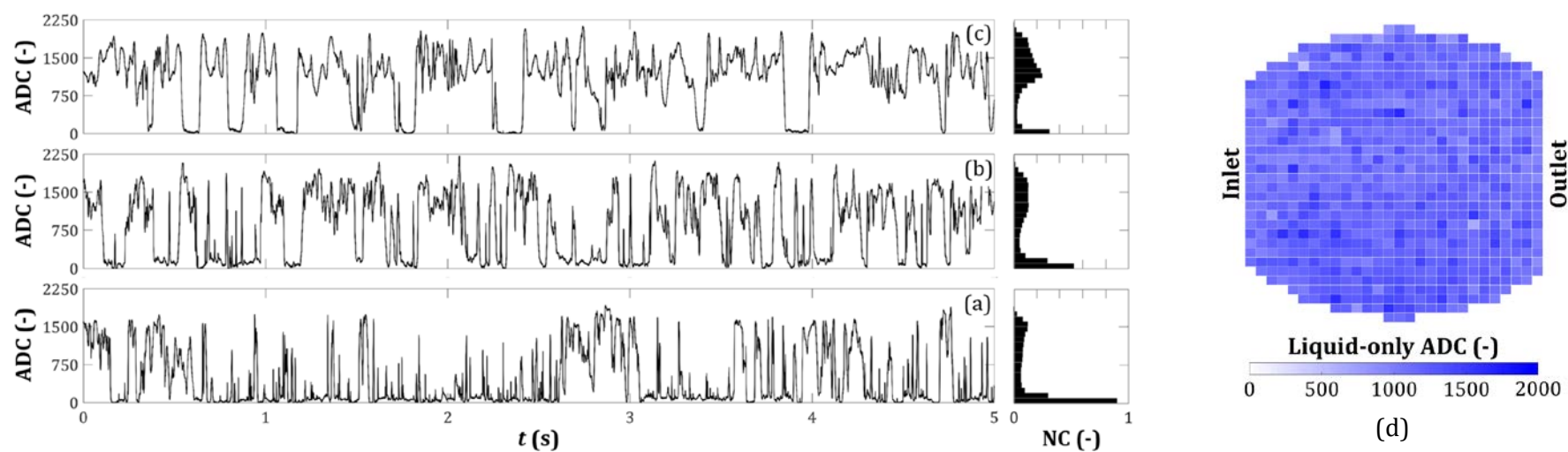
**Figure 4.** Digital data of the probe [17,17] at (a) 20 mm, (b) 40 mm, and (c) 60 mm elevation (NC stands for normalized count here); (d) liquid-only ADC values.
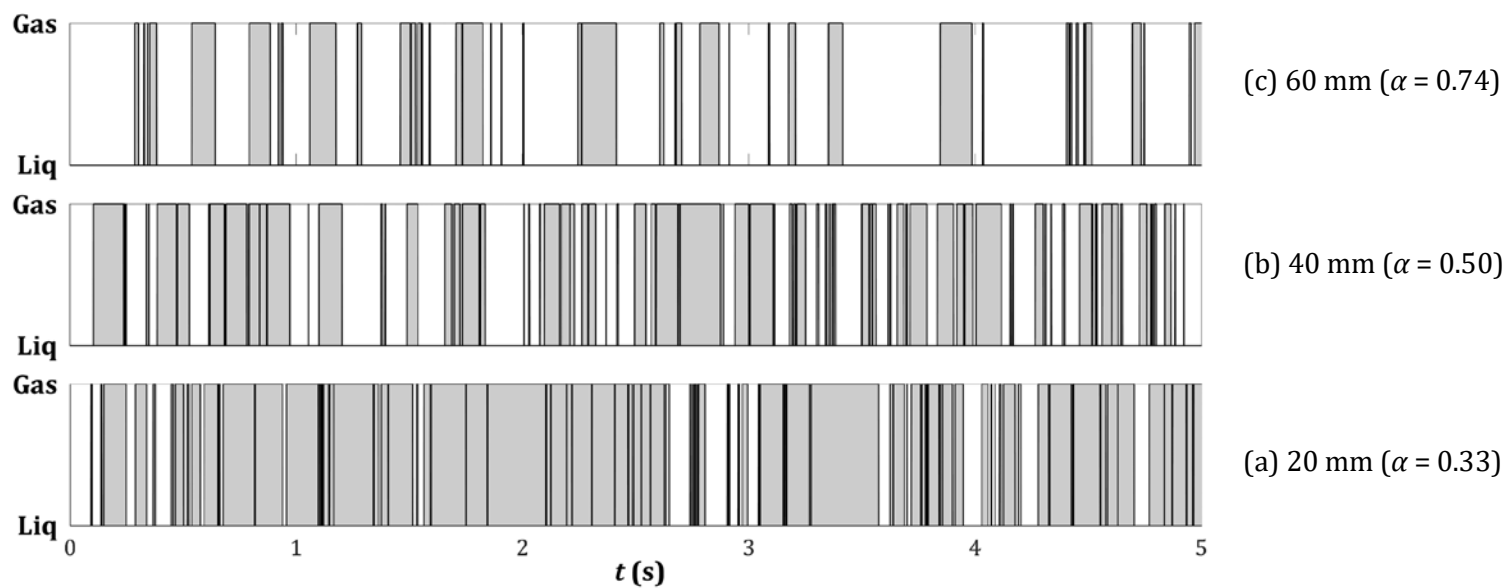


**Figure 5.** Signal binarization for the probe [17,17] at (a) 20 mm, (b) 40 mm, and (c) 60 mm elevation above the tray.

bulk liquid projected up by the gas jets from lower elevations reaches the maximum elevation. This causes an even distribution of liquid and gas in the probe vicinity at 40 mm elevation. Fig. 5c shows a higher liquid content at 60 mm elevation, where the rapid recirculating liquid lamellae and droplets settle and fall from the probe randomly. The supporting evidence for explaining the observations in Fig. 5 are directly derived from another literature study.[18]

## 4.5. Holdup evaluation

Fig. 6 shows exemplarily the local liquid holdup distribution at different elevations above the tray. An increase in the liquid holdups with the elevation is obtained as already explained above. However, the first three probe columns (i.e., parallel and next to the inlet weir) display different holdup behavior up to 40 mm elevation (refer to Figs. 6a–c) than the rest. The first probe column is positioned over the inlet calming zone, and is least exposed to the gas flow. Coincidentally, the resistance offered by the inlet weir (i.e., 35 mm high) to the downcomer backup forms a liquid nappe that overwhelms the first two probe columns at 20 mm elevation. The entering liquid also directs the gas flow from the first line of holes towards the third probe column leading to the local liquid deficiency there. Moreover, the first probe column remains in the liquid rich environment up to 40 mm elevation, while the remaining two columns start exhibiting the increasing holdup trend from 30 mm onwards.

Based on the literature,[18] liquid holdup fractions right above the holes are lower than those above blank spaces between them. This holds only for the measuring planes close to the tray deck, whereas the holdup distribution homogenizes beyond a certain elevation. Accordingly, a non-uniform holdup distribution is observed at 20 mm elevation (see Fig. 6a), since many probes lie above the holes. The holdup distribution homogenizes between 30 mm and 40 mm elevation (refer to Figs. 6b–c). From 50 mm elevation onwards, the holdup distribution regains non- uniformity as shown in
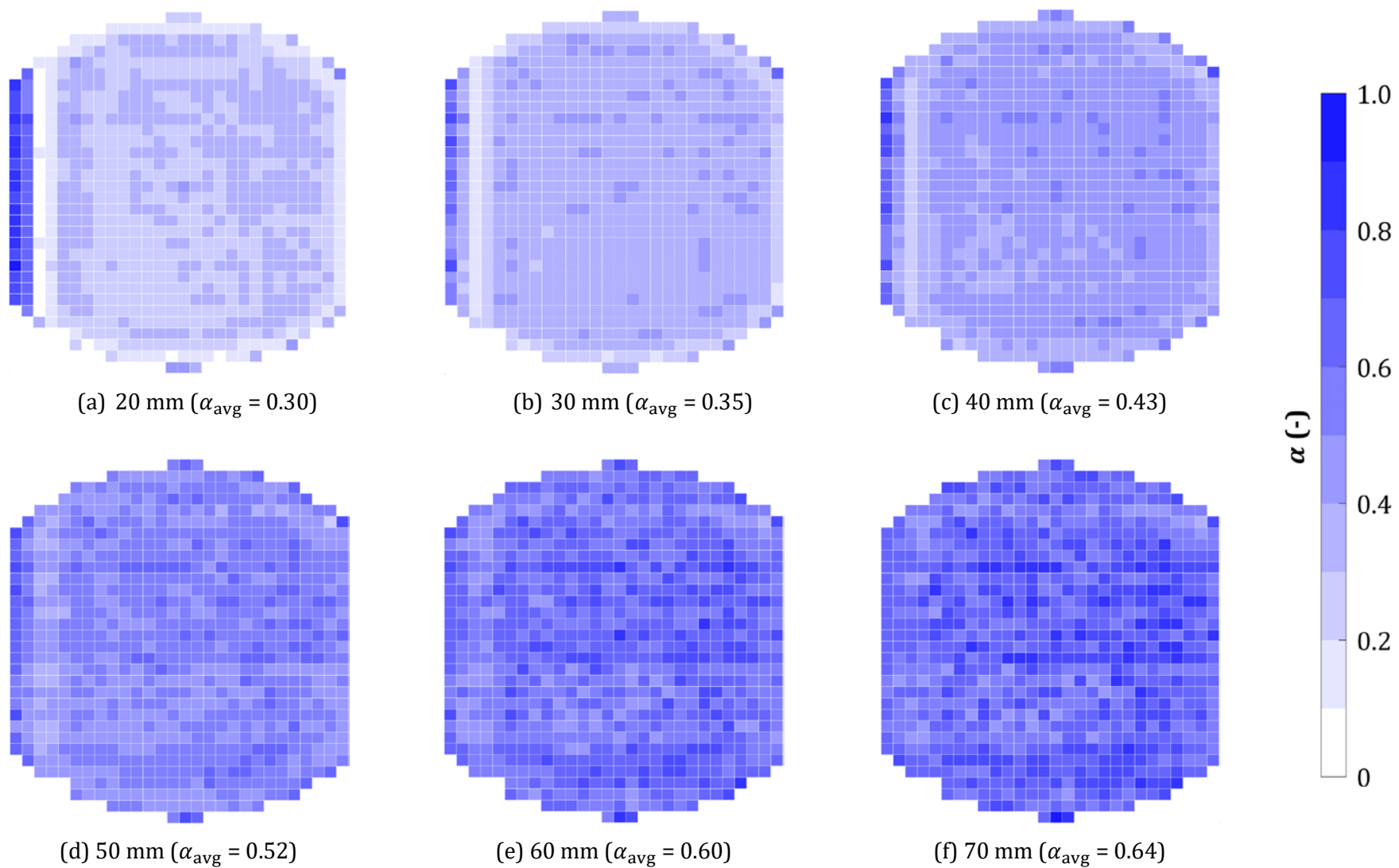
(a) 20 mm ($\alpha_{avg}$ = 0.30)  (b) 30 mm ($\alpha_{avg}$ = 0.35)  (c) 40 mm ($\alpha_{avg}$ = 0.43)

(d) 50 mm ($\alpha_{avg}$ = 0.52)  (e) 60 mm ($\alpha_{avg}$ = 0.60)  (f) 70 mm ($\alpha_{avg}$ = 0.64)

**Figure 6.** Liquid holdup distribution at different elevations above the tray along with the average holdup values. (left edge – tray inlet, right edge – tray outlet)

Figs. 6d–f, because of the liquid lamellae and droplets settling and falling from the probes stochastically. Irrespective of such distribution, the average liquid holdup is nearly constant beyond that elevation (refer to Table S1 in Section S2 of the Supplementary Information).

To confirm data reproducibility, the data time-series signal of the 300 s total sampling time at every profiler elevation was partitioned into three independent samples of 100 s duration each. The average liquid holdups for each sample are given in Table S1 in Section S2 of the Supplementary Information together with the holdup values for the total sampling time. This table justifies the robustness of the holdup measurement and calculation, since the given values are consistent for every profiler elevation irrespective of the sampling duration.

## 5. Liquid flow tracking

Fig. 7 illustrates the series of steps to characterize the liquid velocity and mixing profiles on the tray. This procedure consists of two sets of experiments namely reference experiment and stimulus-response experiment. The reference experiment begins with the two-phase time-series data acquisition, while maintaining the conductivity of the liquid (similar to Fig. 4). This step is repeated for different liquid conductivities and the resulting data are filtered out for extracting the signal fragments related to the liquid flow only. This permits obtaining a unique relationship between the filtered signal and the liquid conductivity over a certain conductivity range for each probe referred to as ADC value – conductivity ($\kappa$) coupling. The stimulus-response experiment commences with the pulse input of tracer in the upstream liquid and the recording of the two-phase digital data simultaneously. Then, the recorded data are filtered and smoothed followed by approximating the individual probe responses using curve fitting. The approximated time-series data are restructured and normalized that enables tracking the timeline and mixing of the tracer-tagged liquid flow. In both experiments, the

profiler elevation is selected as 40 mm, because the two-phase cross-flow near that elevation repre-

sents the effective froth behavior on the tray as observed in Section 4.5.
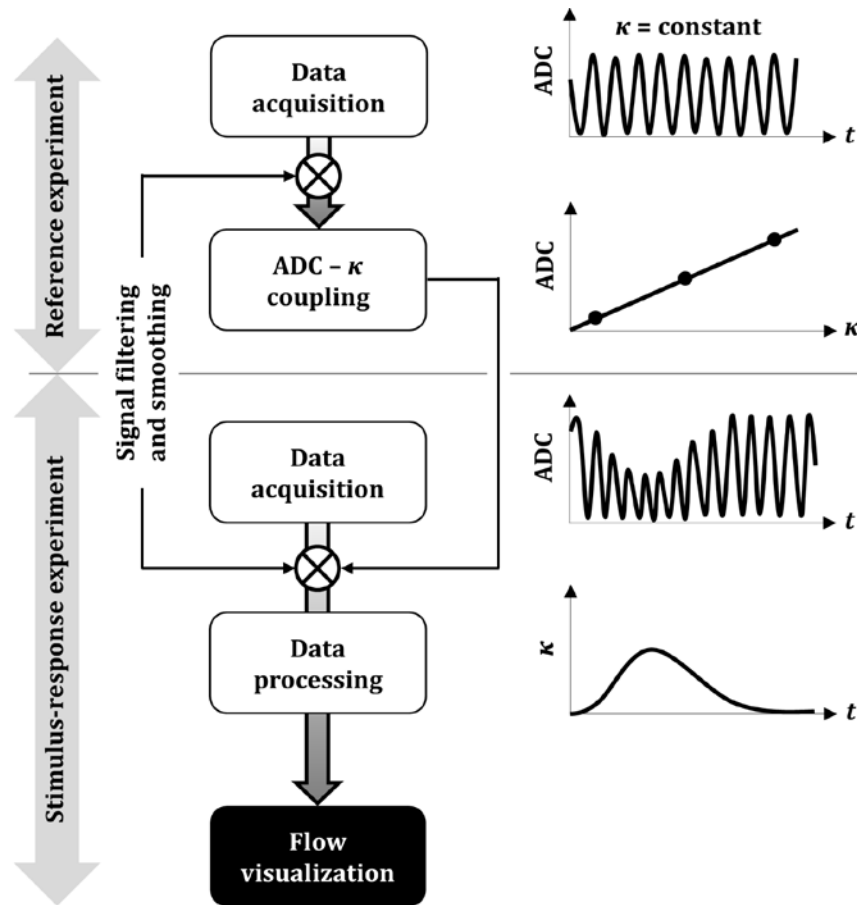


**Figure 7.** Sequence of steps for the liquid flow visualization.

## 5.1. Reference experiment

### 5.1.1 Data acquisition

Three different liquid streams comprising deionized water, tap water, and a combination of both are

supplied serially to the column top. The liquid and gas loadings are identical to those during the

holdup measurements. Once the column attains steady state and the liquid temperature on the tray

16

becomes uniform (i.e., 16.2 °C approximately), the two-phase ADC values are recorded at maximum frequency (i.e., 5000 Hz) for the duration of 60 s. A distribution of recorded data obtained for the probe [17,17] for every conductivity sample is shown in Fig. 8 in terms of box plots. The recorded data are further processed using proper filtering and smoothing schemes to extract the ADC values corresponding to the liquid flow. The application of these schemes on the data gathered with the probe [17,17] for tap water is demonstrated in Section S3 of the Supplementary Information.
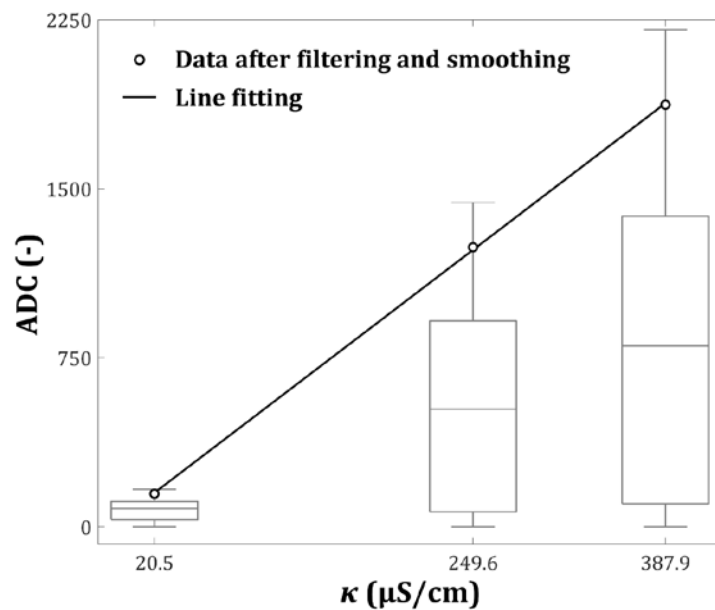


**Figure 8.** ADC data versus liquid conductivity for the probe [17,17].

### 5.1.2 ADC – conductivity coupling

Fig. 8 pinpoints the processed ADC data of the probe [17,17] after filtering and smoothing for the given liquid conductivities. A linear relation couples the processed data and the liquid conductivities. Such behavior holds for every probe of the profiler. It should be noted that such coupling is only valid for the liquid conductivity ranging between that of deionized and tap water (i.e., 20 – 390 μS/cm) here.
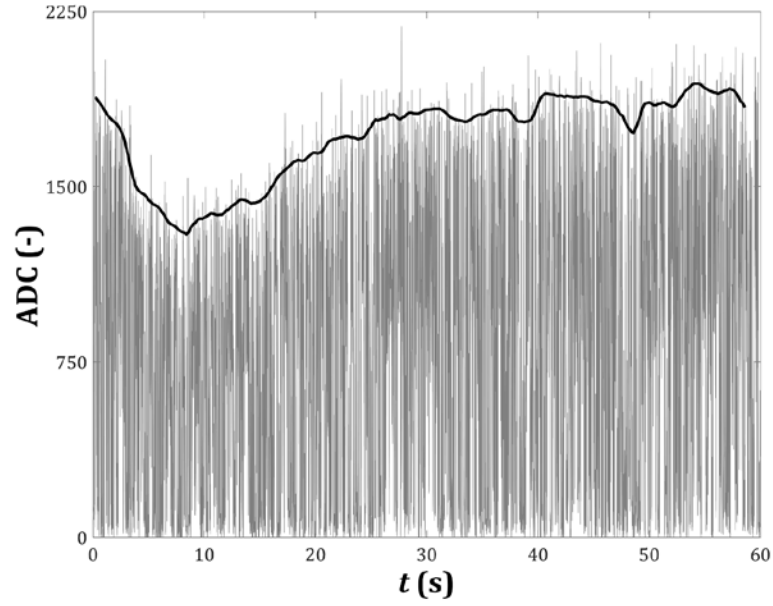
(a)
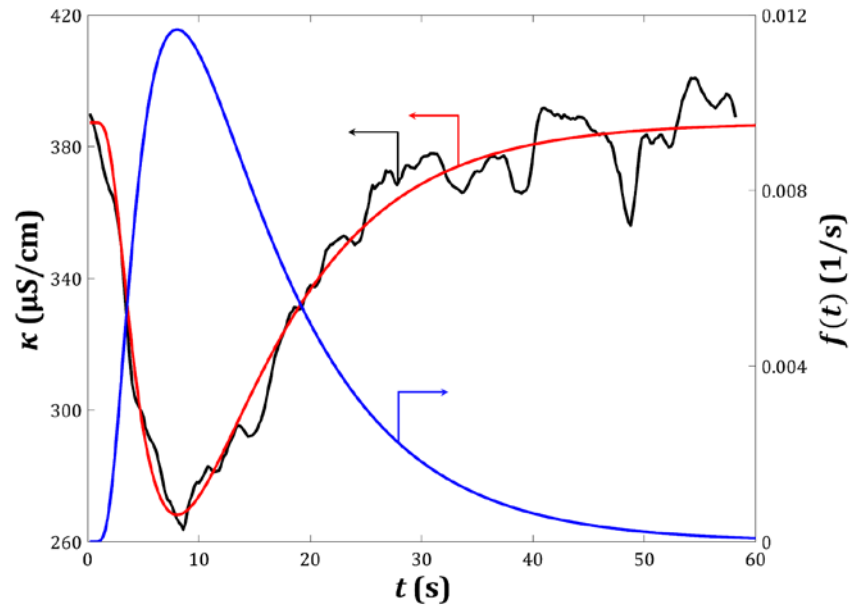


(b)

**Figure 9.** (a) ADC time-series (gray – unfiltered, black – processed) for the probe [17,17], (b) conductivity profiles (black – corresponding to the processed signal, red – fitted function (with $a = 387.33$, $b = $ -10209.34, $c' = 51.48$, $d = 51.46$)) with tracer response function in blue color.

18

## 5.2. Stimulus-response experiment

### 5.2.1 Data acquisition

In the stimulus-response experiments, the operational settings of the column, the profiler elevation, and the data acquisition particulars are the same as those in preliminary experiment with tap water (see Section 5.1.1). As mentioned in Section 2, the tracer (deionized water) is injected into the main liquid (tap water) stream entering the tray near the downcomer clearance. The duration of the tracer injection is 2 s here. Three experimental replicates were sufficient to ensure data reproducibility as discussed below in Section 5.2.2. Subsequently, the data pertaining to each replicate are filtered and smoothed according to the schemes provided in Section S3 of the Supplementary Information. An example of one such replicate is shown in Fig. 9a depicting the primary (i.e., unfiltered) and processed (i.e., filtered and smoothed) signals for the probe [17,17]. Based on the ADC value – conductivity coupling in Section 5.1.2, the evolution of the liquid conductivity (with a temporal resolution of 0.2 s) after tracer injection corresponding to the processed signal is presented in Fig. 9b.

### 5.2.2 Data processing

Minor fluctuations are still visible in the conductivity profile in Fig. 9b. To approximate such profile with a smooth function, the curve fitting approach based on the axial-dispersion model (ADM) is used here. The profiler probes perform point measurements, because the detection volume of their tips is very small compared to the total liquid volume on the tray.[13] The liquid flow itself is largely undisturbed in the local control volumes and over the tray due to the low intrusiveness of the electrode tips. Hence, the open-open boundary condition applies to every measurement point in the ADM,[36] and the corresponding model solution is

$$f(t) = \frac{1}{\sqrt{4\pi t \tau_h N_{TD}}} \cdot \exp\left\{-\frac{(1 - t/\tau_h)^2}{4t N_{TD}/\tau_h}\right\} \quad . \tag{3}$$

In Eq. 3, $f(t)$, $\tau_h$ and $N_{TD}$ are the residence time distribution (RTD) function, hydraulic time and dispersion number, respectively. Their collective descriptions can be found elsewhere.[3,7] The definition of the RTD function during pulse tracer injection is

$$f(t) = \frac{c(t)}{\int_0^\infty c(t)dt} = \frac{\kappa(t)}{\int_0^\infty \kappa(t)dt} \quad , \tag{4}$$

where $c(t)$ is the time history of the tracer concentration. At any instant, the tracer concentration is the amount of total dissolved salts (TDS) in the liquid, which is linearly related to the conductivity within the given range.[37] Thus, the RTD function is defined in terms of liquid conductivity in Eq. 4. Based on Eqs. 3 and 4, the conductivity time-series can be approximated using

$$\kappa(t) = a + b \cdot \left[ \sqrt{\frac{c'}{\pi d^2 t}} \exp\left\{ -\frac{c'}{t}\left(1 - \frac{t}{d}\right)^2 \right\} \right] \quad , \tag{5}$$

where the coefficients $a$, $b$, $c'$, and $d$ are obtained via non-linear least squares curve fitting in MATLAB (R2017b). The fitted function illustrates a good agreement with the target profile in Fig. 9b. The corresponding $f(t)$ is also shown in the same figure after flipping the fitted function vertically and setting its starting point to origin. The function $f(t)$ contains the axial dispersion information for the flow path between the location of tracer injection and the measuring tips of the probe. Finding this function for the local control volume of every probe is infeasible. As this function conveys the time distribution of the tracer appearance at the probe tips, it is referred to as appearance time distribution (ATD) function. Apart from naming, the ATD and RTD functions are the same as defined in Eq. 4, and hence, they are designated by the same nomenclature. Similar to RTD,[38] the ATD function is characterized by the mean appearance time (MAT or $\tau$) and variance ($\sigma^2$) as

$$\tau = \int_0^\infty t \cdot f(t)dt \quad \text{, and} \tag{6}$$

$$\sigma^2 = \int_0^\infty (t - \tau)^2 \cdot f(t)dt \quad \text{, respectively.} \tag{7}$$

Computing the MAT and variance for each probe allows visualizing the flow and mixing patterns of liquid on the tray, respectively. The data recorded by each probe in all three experimental replicates are subjected to these computations. Furthermore, local unidirectional liquid velocities are also calculated by dividing the longitudinal distance between any two probes in a row with the difference in the corresponding MATs.[15]

To assess the data reproducibility, it is recommended to compare the values of MAT and variance for each measuring probe rather than comparing their entire ATDs.[15,38] The average deviation between the replicates for all probes is 4.1% for MAT and 10.9% for variance. Thus, the experimental replicates exhibit a sufficient degree of data reproducibility.

### 5.2.3 Flow visualization

Fig. 10a displays exemplarily the liquid conductivity distribution over the tray during tracer passage at given time intervals (only shown for one experimental replicate). It should be noted that the instantaneous conductivity distribution for the complete duration is provided as video in the Supplementary Information. Figs. 10b and c show the distributions of point MAT and variance over the tray, respectively, where the parameters corresponding to each probe are averaged from all experimental replicates. Fig. 10d depicts the unidirectional liquid velocities exemplarily at five equidistant planes parallel to the weirs, where the lengths of the arrows represent the velocity magnitudes. The distance between two probes in a row (i.e., 84 mm) is divided by the difference between their corresponding MATs (see Fig. 10b) for calculating the unidirectional velocities. Fig. 10 altogether demonstrates that the liquid flow characteristics are symmetric with respect to the longitudinal axis (i.e., centerline) of the tray. This observation has been reported by multiple other studies mentioned in the Table 1. Secondly, the curved wall of the segmental downcomer tends to push the liquid nappe from the column top towards the central part of the downcomer apron. This results in the parabolic velocity distribution in a certain region right after the tray inlet with relatively higher
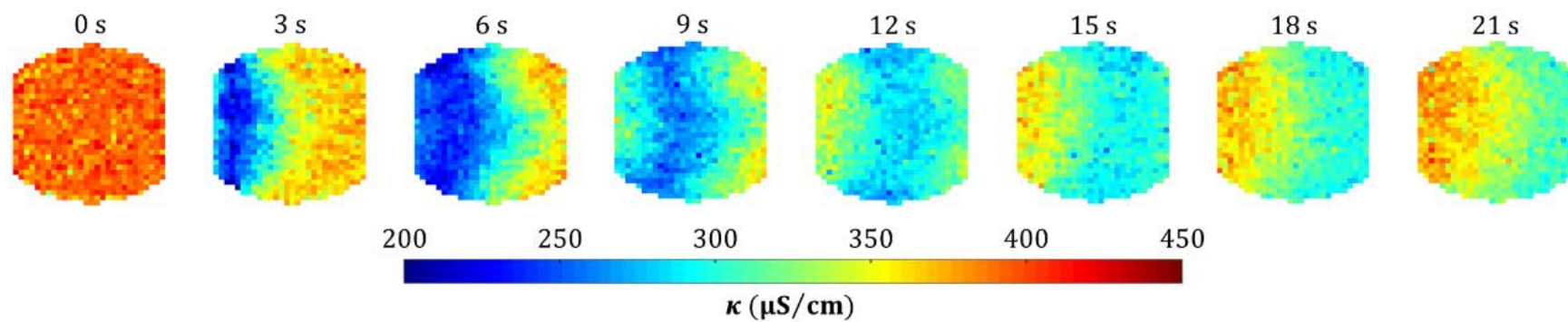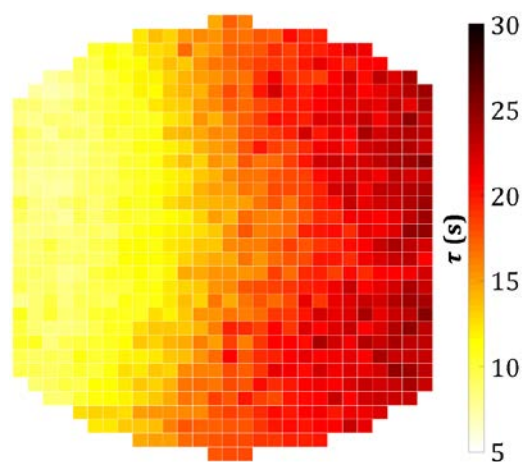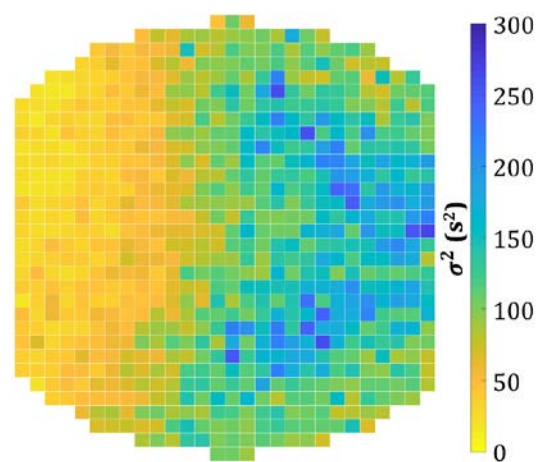
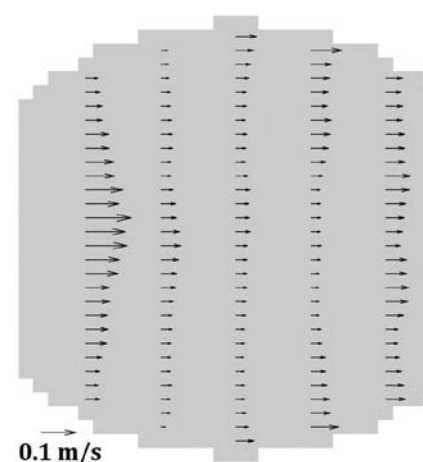**Figure 10.** (a) Snapshots of the tracer passage on the tray at given intervals, (b) point MAT distribution, (c) variance distribution, (d) unidi-

rectional liquid velocity profiles over the tray (left edge – tray inlet, right edge – tray outlet).

liquid velocities along the tray centerline (see Figs. 10a,d).[23] The point MATs and the variances are hence lower in that region as shown in Figs. 10b and 10c, respectively. Coincidently, the rapid vapor flow through the tray deck resists and agitates the traversing liquid. As a result, the liquid flow slows down and the velocity profiles become flatter (see Fig. 10d) owing to high turbulence.[6] The flow resistance and the turbulent mixing leads to higher point MATs and variances in the second half of the tray in Figs. 10b and 10c, respectively. Furthermore, the wall curvature near the outlet weir narrows down the flow passage, which moderately increases the liquid velocity before the tray outlet as illustrated in Fig. 10d. Overall, the liquid velocity is largely uniform over the tray at the given loadings. Therefore, the analytical models[4] considering uniform unidirectional flow with superimposed eddy mixing would reasonably predict the flow parameters and the tray efficiency.

## 6. Conclusion

A new multiplex flow profiler comprising multiple dual-tip probes for simultaneous local conductivity measurements on large-scale distillation trays has been proposed in this work. In particular, the profiler design, electronic scheme, principle of measurement, reference framework, and data processing schemes have been explained in detail. A DN800 air/water column simulator housing sieve trays has been used in this study. A 3D distribution of the time-averaged liquid holdup over the tray at high resolution has been examined. The profiler successfully distinguishes between liquid-continuous and gas-continuous flow in local control volumes pertaining to every measuring probe. A non-uniform holdup distribution has been observed along the dispersion height. Furthermore, the flow and mixing patterns of liquid in the two-phase dispersion over the tray have also been visualized via pulse tracer injection. The liquid velocities were found to be uniform over the entire deck, except near the inlet with the overall liquid flow being symmetric with respect to the tray centerline. The new comprehensive two-phase cross-flow data will enable predicting the tray efficiency accurately, and developing

23

and validating CFD models that have so far largely relied on low-resolution RTD data available in the literature. Although exemplified for sieve trays, minor adjustments would make the profiler suitable for other tray designs and hardware.

Future developments will focus on statistical techniques for extracting the two-phase dispersion parameters from digital data. Extending the current progress to higher column loadings will lead to exhaustive characterization of the tray hydrodynamics, which can be used as an additional benchmark for CFD studies.

## Funding

## Nomenclature

$a, b, c', d$      Coefficients in Eq. 5 (-)

$c(t)$      Time-dependent tracer concentration (mol/m³)

$f(t)$      RTD or ATD function (s⁻¹)

$g_{\text{total}}$      Total number of frames (= $t_{\text{total}}$ × frequency) (-)

$N_{\text{TD}}$      Tray dispersion number (-)

$t$      Time (s)

$t_{\text{total}}$      Total measurement time (s)

$x$      Row index of the probe (-)

$y$      Column index of the probe (-)

| $z$ | Time instances of gas contact with the probe (-) |

## Greek Letters

| $\alpha$ | Time-averaged liquid holdup (-) |
| $\varepsilon$ | Time-averaged gas holdup (-) |
| $\kappa$ | Liquid conductivity ($\mu$S/cm) |
| $\sigma^2$ | Second central moment of $f(t)$ (s$^2$) |
| $\tau$ | Mean appearance time (s) |
| $\tau_{\mathrm{h}}$ | Hydraulic or space time (s) |

## Abbreviations

| ADC | Analog-to-digital converter |
| ADM | Axial dispersion model |
| ATD | Appearance time distribution |
| CT | Computed tomography |
| MAT | Mean appearance time |
| PCB | Printed circuit board |
| RTD | Residence time distribution |

# References

1.  Zhao H, Li Q, Yu G, Dai C, Lei Z. Performance analysis and quantitative design of a flow-guiding sieve tray by computational fluid dynamics. *AlChE J.* 2019;65(5).

2.  Hirschberg S, Wijn E, Wehrli M. Simulating the two phase flow on column trays. *Chem Eng Res Des.* 2005;83(12):1410-1424.

3.  Vishwakarma V, Schubert M, Hampel U. Development of a refined RTD-based efficiency prediction model for cross-flow trays. *Ind Eng Chem Res.* 2019;58(8):3258-3268.

4.  Vishwakarma V, Schubert M, Hampel U. Assessment of separation efficiency modeling and visualization approaches pertaining to flow and mixing patterns on distillation trays. *Chem Eng Sci.* 2018;185:182-208.

5.  Schubert M, Piechotta M, Beyer M, Schleicher E, Hampel U, Paschold J. An imaging technique for characterization of fluid flow pattern on industrial-scale column sieve trays. *Chem Eng Res Des.* 2016;111:138-146.

6.  Biddulph MW, Bultitude DP. Flow characteristics of a small-hole sieve tray. *AIChE J.* 1990;36(12):1913-1916.

7.  Vishwakarma V, Rigos N, Schubert M, Hampel U. Efficiency estimation of tray columns based on flow profiles and vapor–liquid equilibrium characteristics of binary mixtures. *Ind Eng Chem Res.* 2019;58(51):23347-23358.

8.  Górak A, Sorensen E. *Distillation: fundamentals and principles.* Academic Press; 2014.

9.  Malvin A, Chan A, Lau PL. CFD study of distillation sieve tray flow regimes using the droplet size distribution technique. *J Taiwan Inst Chem Eng.* 2014;45(4):1354-1368.

10. Lockett MJ. *Distillation tray fundamentals.* Cambridge University Press; 1986.

11. Hofhuis PAM. *Flow regimes on sieve-trays for gas/liquid contacting*, Technische Hogeschool Delft; 1980.

12. Kister HZ, Haas JR, Hart DR, Gill DR. *Distillation design.* Vol 1: McGraw-Hill New York; 1992.

13. Bell RL. Experimental determination of residence time distributions on commercial scale distillation trays using a fiber optic technique. *AlChE J.* 1972;18(3):491-497.

14. Porter KE, Lockett MJ, Lim CT. The effect of liquid channeling on distillation plate efficiency. *Trans Inst Chem Eng.* 1972;50(2):91-101.

15. Solari RB, Bell RL. Fluid flow patterns and velocity distribution on commercial-scale sieve trays. *AIChE J.* 1986;32(4):640-649.

16. Bernard J, Sargent R. The hydrodynamic performance of a sieve plate distillation column. *Trans Instn Chem Engr.* 1966;44:314-327.

17. Raper JA, Kearney M, Burgess J, Fell C. The structure of industrial sieve tray froths. *Chem Eng Sci.* 1982;37(4):501-506.

18. Pinczewski W, Fell C. Nature of the two-phase dispersion on sieve plates operating in the spray regime. *Trans Inst Chem Eng.* 1974;52(3):294-299.

19. Val Pinczewski W, Benke ND, Fell CJ. Phase inversion on sieve trays. *AIChE J.* 1975;21(6):1210-1213.

20. D'Arcy D. *Analysis of sieve tray froths such as occur in heavy water production plants.* Canada1978. AECL-5828.

21. Burgess J, Calderbank P. The measurement of bubble parameters in two-phase dispersions—I: The development of an improved probe technique. *Chem Eng Sci.* 1975;30(7):743-750.

22. Hu B, Yang H-m, Hewitt GF. Measurement of bubble size distribution using a flying optical probe technique: Application in the highly turbulent region above a distillation plate. *Chem Eng Sci.* 2007;62(10):2652-2662.

23. Bell RL. Residence time and fluid mixing on commercial scale sieve trays. *AIChE Journal.* 1972;18(3):498-505.

24. Li Y, Wang L, Yao K. New technique for measuring fluid flow patterns on a multiple downcomer tray. *Ind Eng Chem Res.* 2007;46(9):2892-2897.

25. Porter KE, Yu KT, Chambers S, Zhang MQ. Flow patterns and temperature profiles on a 2.44 m diameter sieve tray. *Chem Eng Res Des.* 1992;70(A):489-500.

26. Biddulph MW, Burton AC. Mechanisms of recirculating liquid flow on distillation sieve plates. *Ind Eng Chem Res.* 1994;33(11):2706-2711.

27. Sohlo J, Kinnunen S. Dispersion and flow phenomena on a sieve plate. *Trans Inst Chem Eng.* 1977;55:71-73.

28. Stichlmair J, Ulbrich S. Liquid channelling on trays and its effect on plate efficiency. *Chem Eng Technol.* 1987;10(1):33-37.

29. Yu KT, Huang J, Li JL, Song HH. Two-dimensional flow and eddy diffusion on a sieve tray. *Chem Eng Sci.* 1990;45(9):2901-2906.

30. Liu C, Yuan X, Yu KT, Zhu X. A fluid–dynamic model for flow pattern on a distillation tray. *Chem Eng Sci.* 2000;55(12):2287-2294.

31. Gesit G, Nandakumar K, Chuang KT. CFD modeling of flow patterns and hydraulics of commercial-scale sieve trays. *AIChE J.* 2003;49(4):910-924.

32. Vishwakarma V, Schleicher E, Schubert M, Tschofen M, Löschau M, Inventors; Helmholtz Zentrum Dresden Rossendorf eV, assignee. Sensor zur Vermessung von Strömungsprofilen in großen Kolonnen und Apparaten. DE1020181245012020.

33. Hampel U, Schubert M, Döß A, et al. Recent advances in experimental techniques for flow and mass transfer analyses in thermal separation systems. *Chem Ing Tech.* 2020;92(7):926–948.

34. Prasser H-M, Böttger A, Zschau J, Gocht T. Needle shaped conductivity probes with integrated micro-thermocouple and their application in rapid condensation experiments with non-condensable gases. *Kerntechnik (1987).* 2003;68(3):114-120.

35. Chanson H. Phase-detection measurements in free-surface turbulent shear flows. *J Geophys Eng.* 2016;13(2):S74-S87.

36. Levenspiel O. *Chemical reaction engineering.* 3rd ed: John Wiley and Sons; 1999.

37. Walton N. Electrical conductivity and total dissolved solids—what is their precise relationship? *Desalination.* 1989;72(3):275-292.

38. Fogler HS, Gürmen MN. *Elements of chemical reaction engineering (online version).* 4th ed: University of Michigan; 2008.